ACS OMEGA

http://pubs.acs.org/journal/acsodf

Article

Efficacious Removal of Organic Contaminants from Water Using a Novel CoO−NiO@MgAl$_2$O$_4$ Nanocomposite

Sondos A. J. Almahmoud,* Soad S. Alzahrani, and Babiker Y. Abdulkhair

Cite This: *ACS Omega* 2025, 10, 11188−11201

Read Online

ACCESS | Metrics & More | Article Recommendations

ABSTRACT: Herein, novel MgAl$_2$O$_4$-based quadruple nanocomposites containing different contents of Co/Ni bimetallic doping were synthesized employing gelatin as a green capping agent. Typically, MgAl$_2$O$_4$ (MgAl$_2$O$_4$-1), 5% NiO−5% CoO@MgAl$_2$O$_4$ (MgAl$_2$O$_4$-2), 2.5% CoO−5% NiO@MgAl$_2$O$_4$ (MgAl$_2$O$_4$-3), and 5% CoO−2.5% NiO@MgAl$_2$O$_4$ (MgAl$_2$O$_4$-4) were synthesized via a one-pot method. The prepared quadruple nanocomposites were characterized by transmission electron microscopy (TEM), energy-dispersive X-ray spectroscopy (EDX), X-ray diffraction (XRD), surface analysis, and Fourier transform infrared spectroscopy (FTIR) spectroscopy. MgAl$_2$O$_4$-1, MgAl$_2$O$_4$-2, MgAl$_2$O$_4$-3, and MgAl$_2$O$_4$-4 exhibited surface areas of 75.4, 118.4, 141.1, and 123.0 m^2 g^{-1}, respectively, and possessed q_t values of 46.8, 60.9, 72.4, and 60.2 mg g^{-1}, respectively, toward the indigo carmine (INCR) dye. The INCR sorption onto MgAl$_2$O$_4$-1, MgAl$_2$O$_4$-2, MgAl$_2$O$_4$-3, and MgAl$_2$O$_4$-4 followed the pseudo-second-order model, and the liquid film diffusion model controlled the INCR sorption onto MgAl$_2$O$_4$-1, MgAl$_2$O$_4$-2, MgAl$_2$O$_4$-3, and MgAl$_2$O$_4$-4 nanocomposites. MgAl$_2$O$_4$-3 was selected as the best sorbent for eliminating INCR, and it exhibited enhanced performance at pH 6.0. The MgAl$_2$O$_4$ q_t value increased proportionally with the INCR concentration (20 to 100 mg L^{-1}), and increasing the temperature affected the sorption positively, indicating endothermic sorption. The Langmuir model best fitted among the tested isotherm models, and it predicted a maximum adsorption capacity of 181.0 mg g^{-1}. MgAl$_2$O$_4$-3 was tested for removing INCR from tap water, groundwater, and seawater at 313 K, and it showed an average efficiency of 97.1%, with a standard deviation of 2.4%.

1. INTRODUCTION

Accessibility to clean drinking water is considered one of the most pressing global issues, and addressing this issue is unavoidable for protecting public health and promoting sustainable development. Although all water pollutants harm the aquatic life and the ecosystem, compared to pharmaceutical pollutants and heavy metals, organic dyes (ORD) possess an additional negative impact of obstructing visible light.[1] Therefore, addressing dye pollution cannot be overstated, considering the paramount role of pure water in maintaining the well being of the humankind, animals, and the ecosystem. The spread of ORDs in water bodies through illegal discharge of industrial and human wastes into aquatic systems is a severe problem worldwide. ORDs have been extensively utilized in various industrial applications, including food, textiles, medicine, cosmetics, plastic, rubber, and paper.[2] Indigo carmine (INCR) ($C_{16}H_8N_2Na_2O_8S_2$, 466.367 g mol^{-1}) has double sodium sulfonate groups which leads to high water solubility.[3] Because of its resistance to high temperatures, oxidizing chemicals, and intense light, INCR has low biodegradability and can bioaccumulate in the environment, potentially disrupting the food chain and causing ecological imbalance.[4] INCR causes severe acute hypotension, skin irritation, and eye discoloration even at concentrations as low as 170 μM; it also decreases marine organisms' reproduction and elevates their mortality rate.[5] Despite the poisonous and carcinogenic nature of INCR, the manufacturers and users disregarding these risks persisted in utilizing this dye in numerous applications.[6] The annual production estimate is 80,000 tons;[7,8] it is mostly consumed by textile industries, and about 30% of it is discharged into water bodies.[8] Although textile is not the only industry utilizing

Received: November 19, 2024
Revised: February 19, 2025
Accepted: March 4, 2025
Published: March 12, 2025

ACS Publications

https://doi.org/10.1021/acsomega.4c10353

INCR, it remains the major contributor to water contamination by INCR. The insufficiency of standard treatment procedures to prevent organic pollutants from entering drinking water has been exposed by detecting ORD in the tap water of certain first-world countries.[9] Most of these procedures had drawbacks, such as handling difficulties, cost infeasibility, toxic radicals, and technical limitations. Hence, affordable, ecologically friendly techniques for eliminating ORD from contaminated water, such as adsorption protocols, generate no secondary contamination.[10] Several sorbents have been tested, including carbon nanofibers, metal oxides, metal/organic frameworks, carbon/metal-oxide nanocomposites, carbon nanotubes, carbon nitride, and activated carbon.[11] The sorbent favorability can be indicated by its ease of preparation, low cost, high adsorption capacity, environmentally friendliness, and fast sorption equilibria.[12] Metal-oxide nanomaterials can meet most of these criteria, with the nanoscale size offering a substantial surface area and diverse electronegativities that are suitable for interacting with diverse ORD structures.[12,13] Several studies have implemented metal-oxide doping to improve the base material's characteristics by altering the doping substance and/or its percentage. In fact, the hydroxides of Al^{3+} and Mg^{2+} have been utilized as antacid pills for medical purposes, while their oxides serve as key components in ceramics. This might emphasize their environmentally friendly and cost-efficient characteristics, respectively.[14] $MgAl_2O_4$ nanocomposites may present potential environmentally friendly and relatively cheap effective candidates for decontaminating water.[15] Several studies advocate that doping with transition-metal oxides can improve base material's characteristics and adsorption properties.[16] The literature indicated that doping nanomaterials with NiO improves its adsorption properties by influencing the adsorption−desorption processes through the d−π overlap.[17] CoO and NiO mixed metal oxides significantly enhance adsorption capacities via structural alterations, charge transfer, and electron transport, making them possibly favorable dopants for improving material sorption capability. Adding NiO and CoO to sorbents improves their structural and morphological features; the alterations include surface reactivity, surface shape, grain size, structural stability, and sorption capabilities.[17,18] Researchers focused on using green capping agents, such as sucrose, dextrose, gelatin (GLN), and several plant extracts. GLN offers several advantages, such as low cost, eco-friendliness, biodegradability, and biocompatibility, which establish it as an environmentally sustainable capping agent.[19] Moreover, amine groups on the gelatin backbone stabilize and prevent aggregation of the nanomaterial, facilitating controlled size distribution and uniform spherical morphology.[20]

This study aimed to prepare a novel $MgAl_2O_4$-based quadruple nanocomposite as a low-cost, environmentally friendly sorbent using gelatin as a green capping agent in a one-pot protocol. The influence of bidopants cobalt (Co) and nickel (Ni) with varying percentages was explored. Typically, $MgAl_2O_4$ ($MgAl_2O_4$-1, as the base material), 5% NiO−5% CoO@$MgAl_2O_4$ ($MgAl_2O_4$-2), 2.5% CoO−5% NiO@$MgAl_2O_4$ ($MgAl_2O_4$-3), and 5% CoO−2.5% NiO@$MgAl_2O_4$ ($MgAl_2O_4$-4) were synthesized. The prepared quadruple nanocomposites were tested for removing INCR as a representative hazardous water contaminant. Then, the sorbent with the highest adsorption capacity was selected for further investigation. The sorbent's solution parameters, kinetics, isotherms, thermodynamics, and performance toward removing INCR from natural water samples were studied.

2. EXPERIMENTAL SECTION

2.1. Materials. Sodium hydroxide and hydrochloric acid (37%) were purchased from Sharlau, Spain. INCR dye and magnesium acetate tetrahydrate were purchased from Fluka, Switzerland. Aluminum nitrate nonahydrate, nickel nitrate, and gelatin (GLN) were purchased from Riedel-de Haën, Germany. Cobalt acetate (Co $(AC)_2$) was bought from Winlab, England.

2.2. Preparation of Nanocomposites. A 10.0 g portion of GLN, 13.41 g of aluminum nitrate nonahydrate, 9.19 g of magnesium acetate tetrahydrate, and 15 mL of distilled water (DW) were transferred to a 500 mL beaker and then heated to 100 °C until the content became clear. The beaker was overheated using a hot plate until GLN carbonization was reached and then dried in an oven at 120 °C for 3.0 h to reduce the movement of the capping agent during the calcination's early stages. The quadruple nanocomposites $MgAl_2O_4$-2, $MgAl_2O_4$-3, and $MgAl_2O_4$-4 were synthesized similarly except for adding specific amounts of $Ni(NO_3)_2.6H_2O$ and $Co(AC)_2$. Then, the $MgAl_2O_4$-1, $MgAl_2O_4$-2, $MgAl_2O_4$-3, and $MgAl_2O_4$-4 nanocomposites were obtained via calcination at a relatively low temperature of 550 °C for a period of 4.0 h, which is long enough to turn the product into oxides without causing agglomeration of small grains into big ones.

2.3. Characterization of Nanocomposites. The structures of $MgAl_2O_4$-1, $MgAl_2O_4$-2, $MgAl_2O_4$-3, and $MgAl_2O_4$-4 nanocomposites were analyzed by scanning electron microscopy/energy-dispersive X-ray spectroscopy (INCAx-act, 51-ADD0069, X-act, Oxford Instruments) and transmission electron microscopy (TEM) (JEM-1400, JEOL, Pleasanton). The TEM experiment was conducted at The Central Research Laboratory, King Saud University. The porosity and surface properties of $MgAl_2O_4$-1, $MgAl_2O_4$-2, $MgAl_2O_4$-3, and $MgAl_2O_4$-4 were examined by utilizing a surface analyzer (ASAP-2020, Micromeritics, Miami). The crystallinity of the $MgAl_2O_4$-1, $MgAl_2O_4$-2, $MgAl_2O_4$-3, and $MgAl_2O_4$-4 nanocomposites was examined using an X-ray diffractometer (Bruker, D8 Advance; Billerica, MA). The average crystal size (D) was determined using the Scherrer equation (eq 1). The lattice parameters (a and c) were determined using eqs 2 and 3, whereas the lattice imperfection (ε) was determined using eq 4.

$$D = \frac{0.9\lambda}{\beta \cos \theta} \tag{1}$$

$$a = \frac{\lambda}{\sqrt{3} \sin \theta} \tag{2}$$

$$c = \frac{\lambda}{\sin \theta} \tag{3}$$

$$\varepsilon = \frac{\beta}{4 \cos \theta} \tag{4}$$

where θ, β, and λ represent Bragg's angle, the peak width at half-maximum, and the source-wavelength line (Cu Kα = 1.5406 Å), respectively.

2.4. Adsorption Studies. The solution parameters affecting the sorption processes were investigated. When

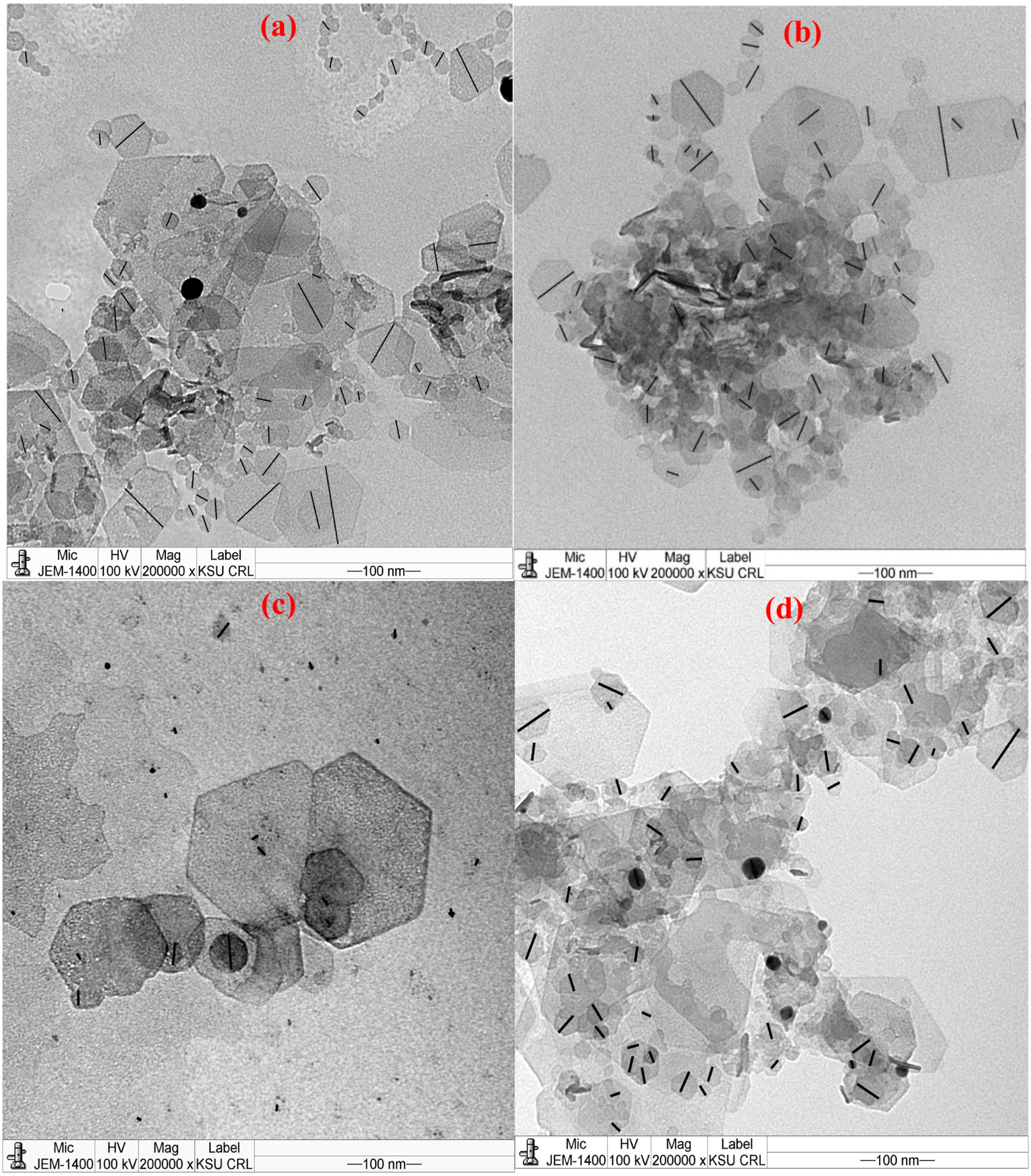

Figure 1. TEM results of (a) $MgAl_2O_4$-1, (b) $MgAl_2O_4$-2, (c) $MgAl_2O_4$-3, and (d) $MgAl_2O_4$-4.

conducting the contact time test, 120 mL of INCR solution (50 mg L^{-1}) was mixed with 50 mg of sorbent. Subsequently, parts of the mixtures were removed at serial intervals until an equilibrium was reached. An ultraviolet−visible (UV−vis) spectrophotometer (UV−vis, Shimadzu-2600i, Tokyo, Japan) was utilized to measure the INCR concentration during the experiments. The adsorption capacity from the contact time investigation was used to investigate the sorption kinetics and to select the best sorbent among the $MgAl_2O_4$-1, $MgAl_2O_4$-2, $MgAl_2O_4$-3, and $MgAl_2O_4$-4 quadruple nanocomposites. Next, INCR concentrations of 20, 40, 60, 80, and 100 mg L^{-1} were utilized to inspect the influence of concentration on the INCR sorption onto the selected best sorbent. The INCR sorption was performed at 293, 303, 313, and 323 K to examine the temperature effect and further investigations, including sorption isotherms and thermodynamics. Furthermore, the

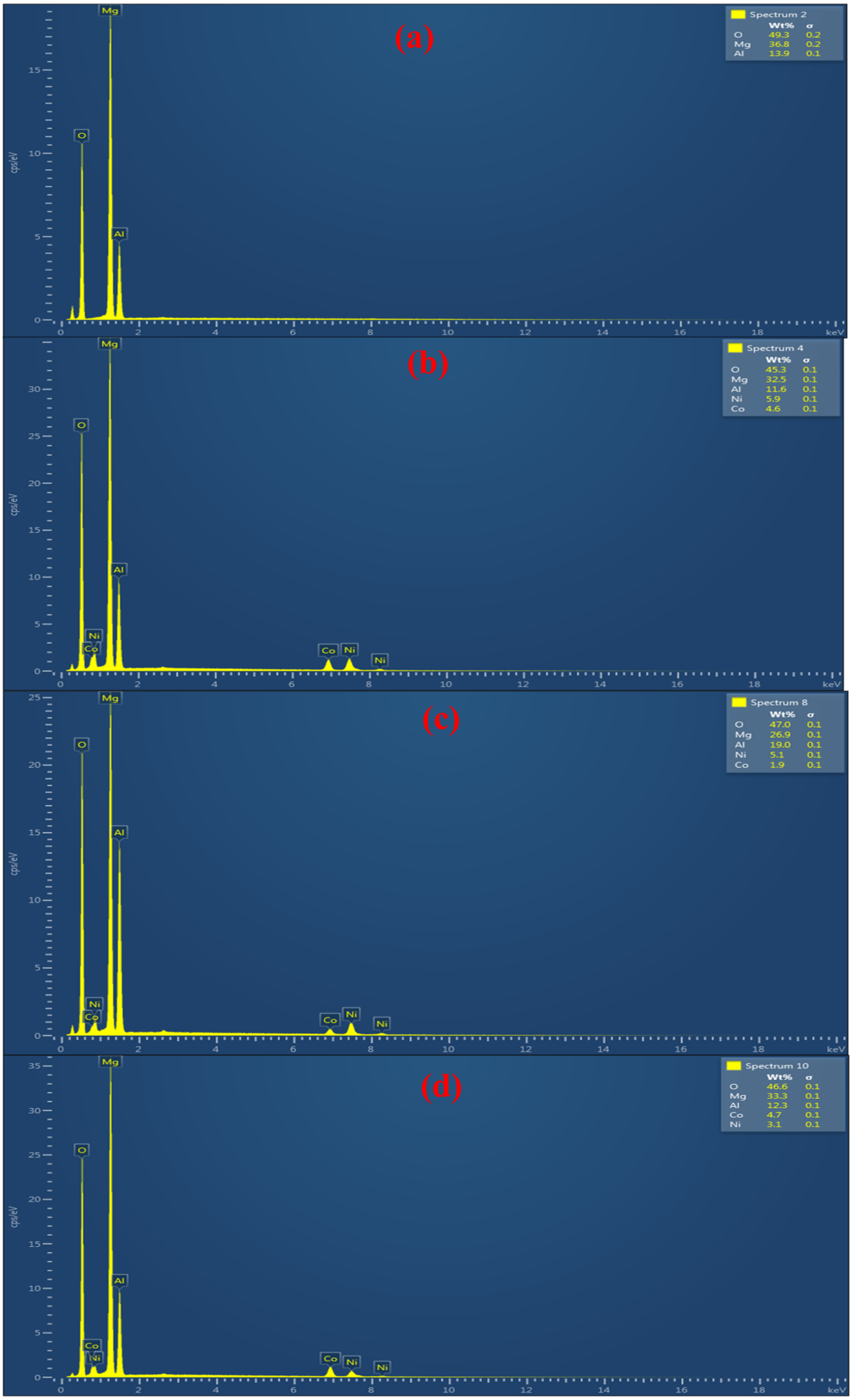

Figure 2. EDX results of (a) $MgAl_2O_4$-1, (b) $MgAl_2O_4$-2, (c)$MgAl_2O_4$-3, and (d) $MgAl_2O_4$-4.

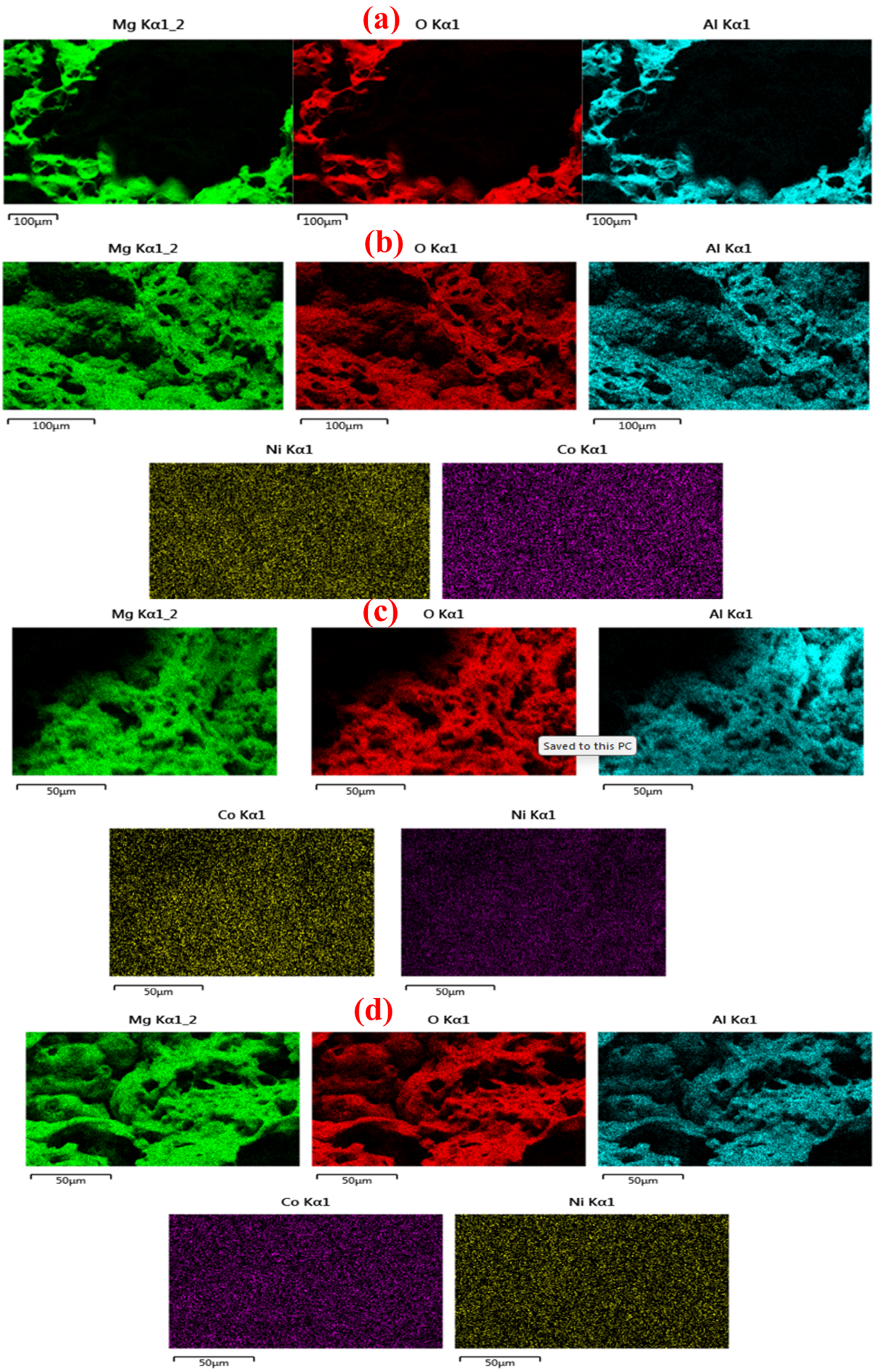

Figure 3. EDX elemental mapping results of (a) $MgAl_2O_4$-1, (b) $MgAl_2O_4$-2, (c)$MgAl_2O_4$-3, and (d) $MgAl_2O_4$-4.

https://doi.org/10.1021/acsomega.4c10353
ACS Omega 2025, 10, 11188−11201

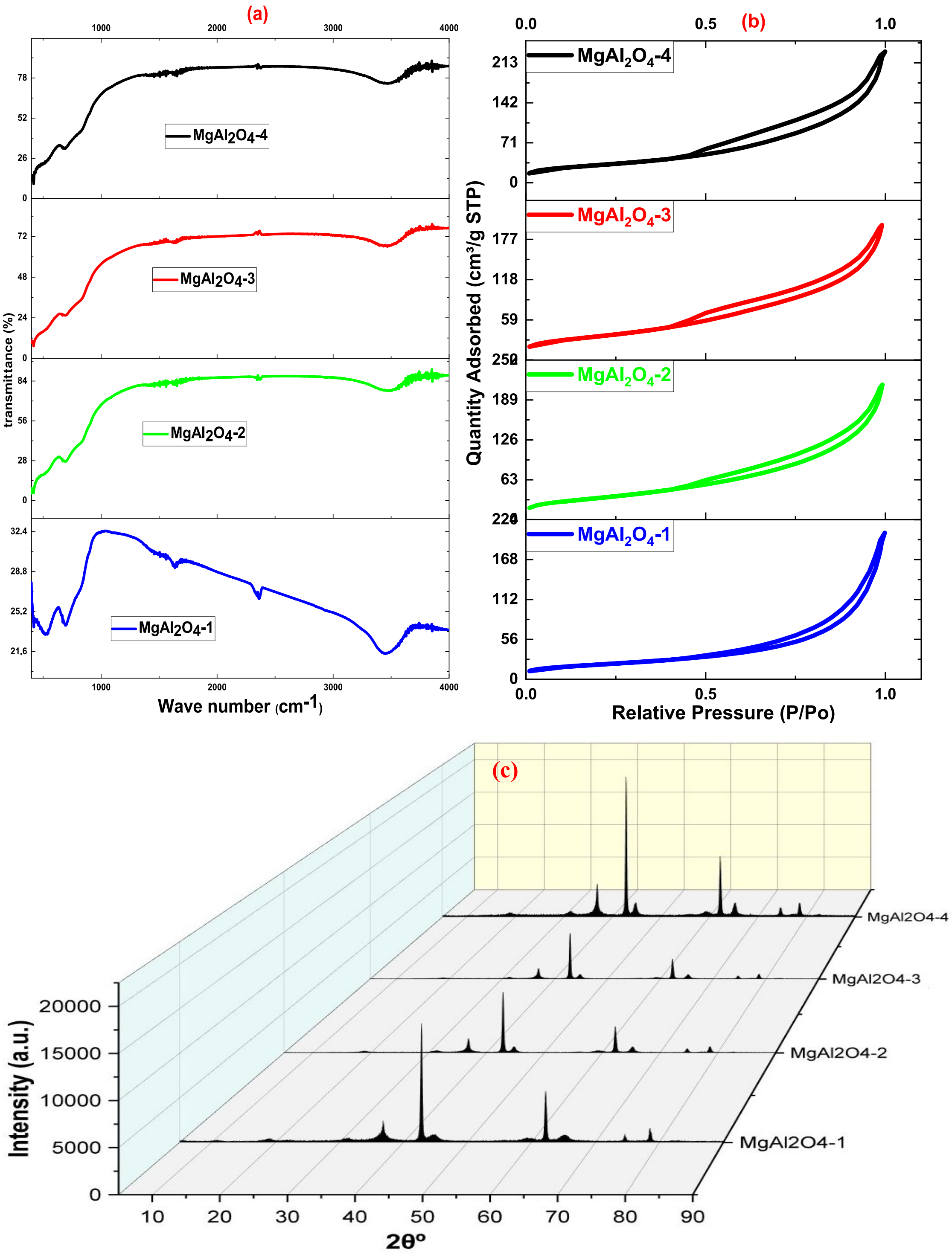

Figure 4. (a) FTIR spectra, (b) N_2 adsorption−desorption isotherms, and (c) XRD results of $MgAl_2O_4$-1, $MgAl_2O_4$-2, $MgAl_2O_4$-3, and $MgAl_2O_4$-4 quadruple nanocomposites.

impact of pH on INCR sorption was surveyed within the pH range of 2.0−10.0. The adsorption percentage and capacity (adsorption % and q_t) were determined via eqs 5 and 6, respectively.

$$\mathrm{Ads\%} = \frac{(C_o - C_t)}{C_o} \times 100 \tag{5}$$

$$q_t = \frac{(C_o - C_t)v}{m} \tag{6}$$

where C_o and C_t (mg L^{-1}) denote the INCR concentration at $t = 0$ and t = t min; v (L) and m (g) represent the solution's volume and sorbent's mass, respectively.

2.5. Application to Natural Water Samples. In order to inspect the robustness and applicability of the best sorbent, it was tested for treating natural water samples. The initial

Table 1. XRD Results of the As-synthesized $MgAl_2O_4$-1, $MgAl_2O_4$-2, $MgAl_2O_4$-3, and $MgAl_2O_4$-4 Quadruple Nanocomposites

parameter		2θ (°)	$MgAl_2O_4$-1	$MgAl_2O_4$-2	$MgAl_2O_4$-3	$MgAl_2O_4$-4
D	peak 1	42.9423	3.6912	4.1674	3.0883	5.6675
	peak 2	62.4233	3.1735	3.1952	3.7936	4.5682
	avg		3.4324	3.6813	3.4410	5.1179
a	peak 1	42.8016	0.0325	0.0328	0.0328	0.0326
	peak 2	62.3195	0.0460	0.0462	0.0462	0.0461
	avg		0.0392	0.0395	0.0395	0.0393
c	peak 1	43.26408	0.4209	0.4222	0.4179	0.4208
	peak 2	62.6287	0.2973	0.2977	0.2964	0.2974
	avg		0.3591	0.3600	0.3572	0.3591
ε	peak 1	42.9519	0.0081	0.0072	0.0097	0.0053
	peak 2	62.4029	0.0080	0.0079	0.0067	0.0056
	avg		0.0081	0.0076	0.0082	0.0054

parameters, such as pH, conductivity, temperature, and total dissolved salts (TDS), were determined for the collected samples of tap water (TaWa), groundwater (GrWa), and seawater (SeWa). Each sample was utilized as a solvent for preparing 5 and 10 mg L^{-1} INCR solutions. The solution/sorbent ratio of 120 mL/50 mg was preserved; each mixture was stirred for the equilibrium time, and then the removal efficiency (%) was calculated.

3. RESULTS AND DISCUSSION

3.1. Characterization. The particle size of the quadruple nanocomposites was analyzed by using the TEM technique (Figure 1). The size of $MgAl_2O_4$-1, $MgAl_2O_4$-2, $MgAl_2O_4$-3, and $MgAl_2O_4$-4 was analyzed via the ImageJ program by measuring 50 particles in their images. The prepared $MgAl_2O_4$-1, $MgAl_2O_4$-2, $MgAl_2O_4$-3, and $MgAl_2O_4$-4 nanocomposites showed the size range of 3.8−28.7, 1.7−26.0, 1.4−13.3, and 2.8−17.6 nm, respectively, with the average particle size of 8.5, 7.6, 2.8, and 6.5 nm, respectively. The $MgAl_2O_4$-3 composition had the most limited size distribution and the smallest mean particle size; this suggests that the 2.5% CoO with 5% NiO dopants resulted in the most favorable $MgAl_2O_4$ composition compared to other investigated nanocomposites.

EDX was utilized to examine the constituting elements and if they were distributed homogeneously in the prepared $MgAl_2O_4$-1, $MgAl_2O_4$-2, $MgAl_2O_4$-3, and $MgAl_2O_4$-4. The resulting spectra in Figure 2 show no foreign element peak except for the minor peak at about 0.5 keV that might be attributed to the trace carbon residue and sample holder carbon grid. The elemental mapping illustrated in Figure 3 indicates that the elemental constituents are homogeneously distributed throughout the tested areas.

Figure 4a illustrates the Fourier transform infrared spectroscopy (FTIR) investigation of the $MgAl_2O_4$-1, $MgAl_2O_4$-2, $MgAl_2O_4$-3, and $MgAl_2O_4$-4 quadruple nanocomposites. The vibrating bands below 1000 cm^{-1} in Figure 4a can be explained as due to Al−O−Al symmetric−asymmetric stretching vibrations and Mg−O, Ni−O, and Co−O bonds. The doublet vibration peaks at 516 and 690 cm^{-1} can be assigned to the Mg−O−Al bond of spinel $MgAl_2O_4$ crystals.[21] The broad bands between 3000 and 3500 cm^{-1} indicate the O−H stretching vibration, possibly of adsorbed water. The $MgOAl_2O_3$-1 FTIR results present two vibration peaks at 1650 and 2200 cm^{-1} that can be assigned to C═C and C≡C stretching vibrations of residual carbonaceous traces from the intermolecular spacer (gelatin) after combustion.

The surface properties of $MgAl_2O_4$-1, $MgAl_2O_4$-2, $MgAl_2O_4$-3, and $MgAl_2O_4$-4 quadruple nanocomposites were explored via N_2 adsorption−desorption. The N_2 isotherm curves were produced by measuring the amount of gas adsorbed as the relative pressure increases. In contrast, the gas released from the sample yields the desorption isotherm when the relative pressure declines. Figure 4b illustrates the generated hysteresis loops of $MgAl_2O_4$-1, $MgAl_2O_4$-2, $MgAl_2O_4$-3, and $MgAl_2O_4$-4. The four quadruple nanocomposites exhibited H3 hysteresis loops indicative of aggregates with mesoporous structures with slit-like pore constructions.[22,23] $MgAl_2O_4$-1, $MgAl_2O_4$-2, $MgAl_2O_4$-3, and $MgAl_2O_4$-4 show surface areas of 75.4, 118.4, 141.1, and 123.0 m^2 g^{-1}, respectively, and average pore sizes of 12.9, 8.3, 7.0, and 0.79 nm, respectively, which might be explained as within clustered pores.

The X-ray diffraction (XRD) methodology was employed to assess the $MgAl_2O_4$-1, $MgAl_2O_4$-2, $MgAl_2O_4$-3, and $MgAl_2O_4$-4 nanocomposites' phase purity (Figure 4c), and the computed lattice parameters are presented in Table 1. The difference in intensity of each nanomaterial across the four samples may provide insight into their crystal size. $MgAl_2O_4$-2, $MgAl_2O_4$-3, and $MgAl_2O_4$-4 exhibit peak intensities of approximately two-thirds of $MgAl_2O_4$-1, indicating larger crystals for the last, which aligns with the TEM findings. Matching the obtained diffraction peaks with the standard PDF card reveals the presence of MgO and spinel $MgAl_2O_4$ phases. The $MgAl_2O_4$ spinel phase was indexed to 2θ values of 18.9, 37.0, 38.9, 45.2, 56.1, 65.01, 74.7, and 78.7. These diffractions are assigned to (111), (311), (222), (400), (422), (440), (620), and (622) planes of the cubic phase of $MgAl_2O_4$ spinel (COD No. 9002164), respectively. The coexistence of the cubic phase of MgO was observed at 2θ values of 37.0, 43.0, 62.4, and 74.7 assigned to planes (111), (200), (220), and (311) (COD No. 9006789), respectively.[24] Furthermore, no prominent peak appeared for the doping substrates, which can be attributed to the minor doping doses or excellent dispersion of both oxides, as illustrated via EDX-mapping results.

3.2. Contact Time and Kinetic Investigations. The contact time influence on INCR removal by $MgAl_2O_4$-1, $MgAl_2O_4$-2, $MgAl_2O_4$-3, and $MgAl_2O_4$-4 nanocomposites is depicted in Figure 5a. Adsorption onto the three sorbents rapidly advanced and achieved equilibrium within a 90 min time frame. $MgAl_2O_4$-1, $MgAl_2O_4$-2, $MgAl_2O_4$-3, and $MgAl_2O_4$-4 exhibited q_t values of 46.79, 60.89, 72.43, and 60.22 mg g^{-1}, respectively, which aligned with the surface area results that can be attributed to the additional pores opened via the insertion of doping substrates within the base nanoma-

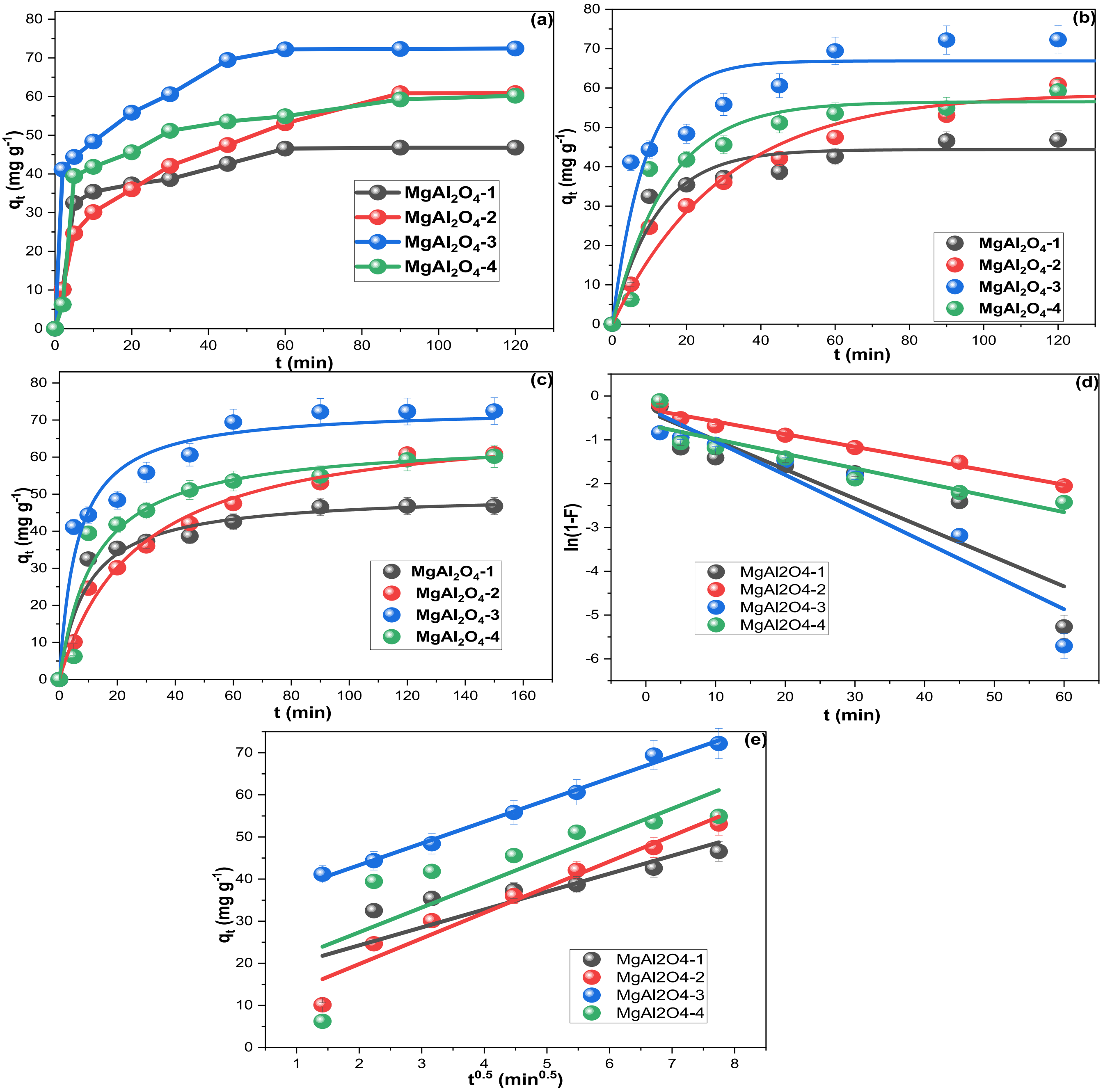

Figure 5. (a) Contact time results, (b) NLPF, (c) NLPS, (d) ID, and (e) LD plots of INCR removal by $MgAl_2O_4$-1, $MgAl_2O_4$-2, $MgAl_2O_4$-3, and $MgAl_2O_4$-4 from 50 mg L^{-1} solution at 20 °C.

terial. It is worth noting that the first 2.0 min sufficed for 10, 20, 60, and 20% of INCR uptake by $MgAl_2O_4$-1, $MgAl_2O_4$-2, $MgAl_2O_4$-3, and $MgAl_2O_4$-4, respectively, indicating the superiority of $MgAl_2O_4$-3 over the other three nanocomposites prepared in this study. Table 2 compares the performance of $MgAl_2O_4$-1, $MgAl_2O_4$-2, $MgAl_2O_4$-3, and $MgAl_2O_4$-4 with the other sorbents in the literature employed for removing INCR.

The contact time outcomes were employed for inspecting the INCR sorption kinetics onto $MgAl_2O_4$-1, $MgAl_2O_4$-2, $MgAl_2O_4$-3, and $MgAl_2O_4$-4. The sorption order was studied utilizing original nonlinear equations of the kinetic model's order: pseudo-first (NLPF, eq 7) and pseudo-second (NLPS, eq 8).[33,34] Furthermore, the diffusion models, liquid film (LD, eq 9) and intraparticle (ID, eq 10), were for inspecting the INCR rate-control mechanism.

$$q_t = q_e(1 - \exp^{-K_1 t}) \tag{7}$$

$$q_t = \frac{k_2 \cdot q_e^{\,2} \cdot t}{1 + k_2 \cdot q_e \cdot t} \tag{8}$$

$$q_t = K_{IP} \cdot t^{1/2} + C_i \tag{9}$$

$$\ln(1 - F) = -K_{LD} \cdot t \tag{10}$$

The rate constants of NLPF and NLPS were denoted by k_1(min^{-1}) and k_2 (g mg^{-1} min^{-1}), respectively, while those of

Table 2. Comparison of $MgAl_2O_4$-1, $MgAl_2O_4$-2, $MgAl_2O_4$-3, and $MgAl_2O_4$-4 with Other Sorbents Utilized to remove INCR in the Literature

sorbent	pollutant	adsorption capacity (mg g^{-1})	refs
$MgAl_2O_4$-1	INCR	46.8	this study
$MgAl_2O_4$-2	INCR	60.9	this study
$MgAl_2O_4$-3	INCR	72.4	this study
$MgAl_2O_4$-4	INCR	60.2	this study
activated carbon	INCR	9.4	25
volcanic ash/AcC	INCR	12.6	26
activated carbon	INCR	17.4	27
activated carbon	INCR	53.8	28
Moringa oleifera seeds	INCR	60.2	29
raw pistachio pods	INCR	15.3	30
$MgAl_2O_3$	methylene blue	243.0	31
$MgAl_2O_4$@CNTs	perfluorooctanoic acid	176.5	32

Table 3. Kinetic Results of INCR Sorption onto $MgAl_2O_4$-1, $MgAl_2O_4$-2, $MgAl_2O_4$-3, and $MgAl_2O_4$-4 Quadruple Nanocomposites

adsorption rate order											
		NLPF					NLPS				
sorbent	q_{max} exp (mg g^{-1})	q_e (mg g^{-1})	K_1	R^2	X^2	RSS	q_e (mg g^{-1})	K_2	R^2	X^2	RSS
$MgAl_2O_4$-1	46.793	44.363	0.083	0.943	16.545	132.360	50.151	0.002	0.953	13.658	109.261
$MgAl_2O_4$-2	60.893	58.677	0.033	0.970	14.515	116.121	70.895	0.001	0.987	6.364	50.908
$MgAl_2O_4$-3	72.435	66.892	0.110	0.891	61.357	490.855	73.383	0.002	0.955	25.088	200.708
$MgAl_2O_4$-4	60.217	56.508	0.068	0.931	35.359	282.870	64.880	0.001	0.933	34.004	272.028

adsorption rate mechanism									
	ID					LD			
sorbent	K_{IP} (mg g^{-1} $min^{1/2}$)	C (mg g^{-1})	R^2	X^2	RSS	K_{LF} (min^{-1})	R^2	X^2	RSS
$MgAl_2O_4$-1	2.968	0.398	0.775	12.448	99.585	0.067	0.831	0.067	2.555
$MgAl_2O_4$-2	2.437	5.101	0.682	13.498	107.987	0.029	0.978	0.066	0.053
$MgAl_2O_4$-3	2.192	8.660	0.708	9.629	77.034	0.077	0.896	0.009	1.929
$MgAl_2O_4$-4	1.819	12.115	0.707	6.664	53.312	0.033	0.841	0.026	0.592

LD and ID were denoted by k_{LF} (min^{-1}) and k_{IP} (mg g^{-1} $min^{-0.5}$), respectively. The slope and intercept of the NLPF and NLPS plots in Figure 5(b),(c) were utilized for computing the k_1 and k_2 magnitude gathered in Table 3. The correlation coefficient (R^2) was regarded as the principal criterion in determining the best-fitted model, with the residual sum of squares and reduced X^2 used as further evaluation parameters.[33] The data extracted from the fittings of the INCR sorption onto the four fabricated sorbents indicated better agreement with the NLPS, where the higher R^2 values were supported by small X^2 values (Table 3). The obtained data indicate the capability of $MgAl_2O_4$-1, $MgAl_2O_4$-2, $MgAl_2O_4$-3, and $MgAl_2O_4$-4 for multilayered adsorption with the sorbed molecules interacting with each other.

Figure 5(d),(e) illustrates the plots of ID and LD for INCR sorption onto $MgAl_2O_4$-1, $MgAl_2O_4$-2, $MgAl_2O_4$-3, and $MgAl_2O_4$-4, respectively. The findings collected in Table 3 show that LD controlled the INCR sorption onto the fabricated quadruple composites with higher R^2 values with X^2 and RSS values lower than those of IP fittings by about 50- to 200-fold. The INCR sorption fitting LD model can be attributed to the high surface area and relatively large pores of $MgAl_2O_4$-1, $MgAl_2O_4$-2, $MgAl_2O_4$-3, and $MgAl_2O_4$-4. Moreover, the C_i values above zero for the four nanocomposites are an additional factor implying the sorption disagreement with the ID model.[23,35] The INCR sorption being controlled by the LD model indicates the high affinity of the pollutant for the quadruple nanocomposites prepared in this study.

3.3. Sorption Equilibria. Based on the contact time output, $MgAl_2O_4$-3 was selected as the best sorbent among the synthesized quadruple nanocomposites. Therefore, the concentration impact on the INCR sorption was inspected using $MgAl_2O_4$-3 as the selected sorbent (Figure 6a). The qt increased proportionally as the concentration increased until 80 mg L^{-1}; then, the line showed significant inflation, indicating the suitability of sorbent's dose (0.417 g sorbent/L contaminated water) to treat up to 80 mg L^{-1}. Increasing the INCR solution temperature from 293 to 323 K increased the sorption efficiency significantly, where the removal of 20 mg L^{-1} INCR shifted from 44 to 96%. These results can be attributed to the disintegration of $MgAl_2O_4$-3 clusters and the creation of virgin active surface sites. Elevating the 100 mg L^{-1} INCR solution temperature lifted the q_t of $MgAl_2O_4$-3 from 58.9 to 110.6 mg g^{-1}, demonstrating that INCR adsorption by $MgAl_2O_4$-3 was endothermic. The results indicated the effectiveness of $MgAl_2O_4$-3 for treating INCR-contaminated effluents with concentrations resembling those of wastewater and industrial wastewater limits. For further understanding the INCR sorption onto $MgAl_2O_4$-3, the Langmuir (LM), Freundlich (FM), and Dubinin−Radushkevich (DRM) isotherm models were investigated utilizing the effect of concentration results at 293 K. The postulation of single-layered sorption with no sorbate−sorbate interaction was

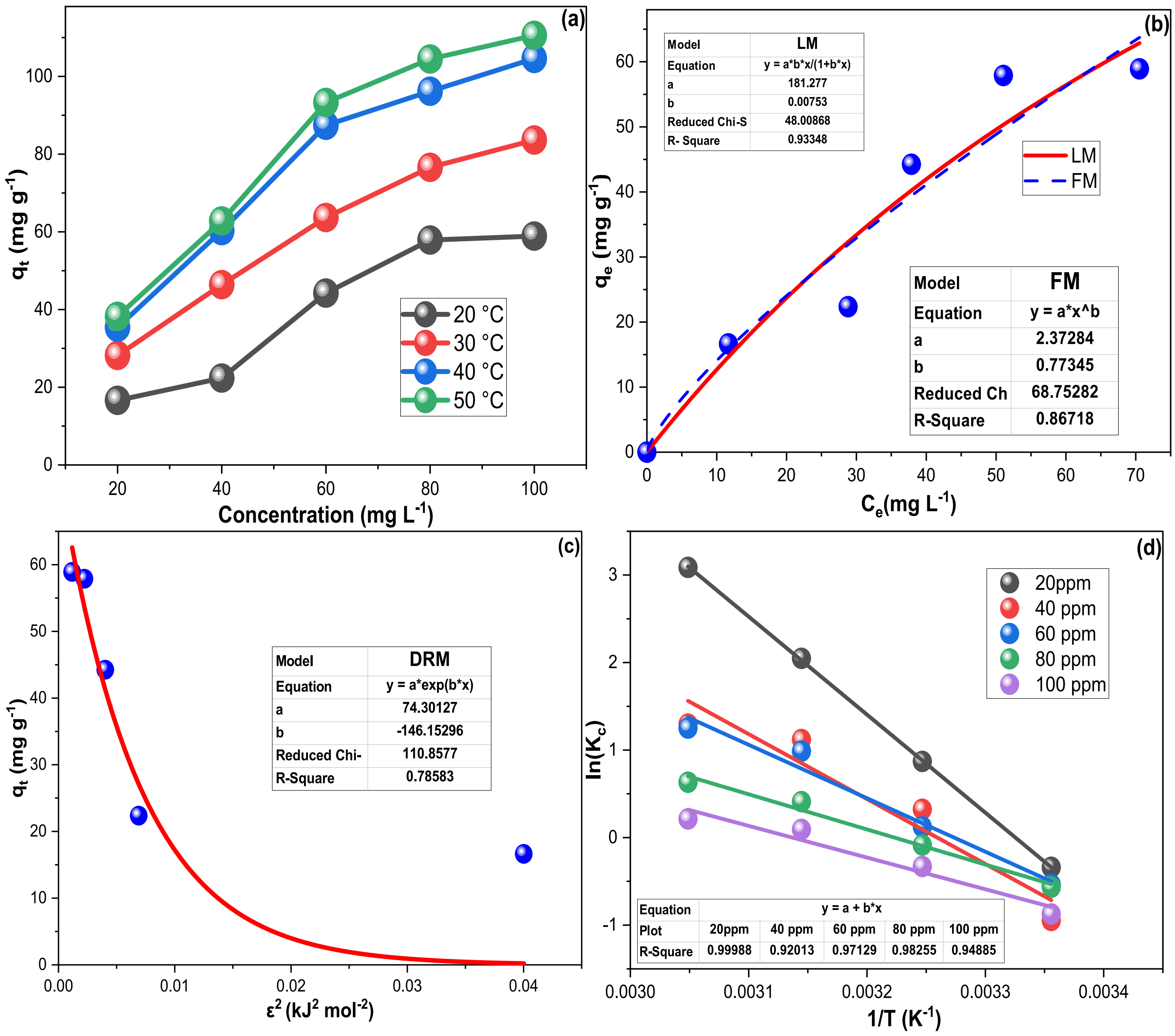

Figure 6. (a) Effect of concentration and temperature on INCR sorption from 20 to 100 mg^{-1} in the concentration range and from 293 to 323 K, (b) LI and FI fittings, (c) DRM plot, and (d) thermodynamic plot from the above-identified concentration and temperature ranges.

investigated using LM (eq 11), the multilayer sorption possibility was inspected via the FM (eq 12), and the DRM (eq 13) was used to determine physisorption/chemisorption nature. The Polanyi potential (ε, kJ mol^{-1}) was computed via eq 14 (ideal gas constant R = 0.0081345 kJ mol^{-1}). At the same time, the energy required to detach an INCR molecule from the $MgAl_2O_4$-3 site to infinity (eq 15) was utilized for computing the Dubinin energy (E_D, kJ mol^{-1}).

$$q_e = \left(\frac{K_l q_m C_e}{1 + q_m C_e}\right) \tag{11}$$

$$q_e = K_F \cdot C_e^{1/n} \tag{12}$$

$$q_e = q_m e^{-K_D \varepsilon^2} \tag{13}$$

$$\varepsilon = RT \ln\left(1 + \frac{1}{C_e}\right) \tag{14}$$

$$E_D = (2K_D)^{-0.5} \tag{15}$$

Here, C_e (mg L^{-1}) is the INCR concentration; q_m is the maximum q_t; K_L (L mg^{-1}) is the LM constant; K_F (L g^{-1}) and $1/n$ are the FM constant and favorability factor, respectively. The Dubinin constant (K_D, kJ^2 mol^{-2}) was driven from the slope.[6,23] Figure 6b monitors the collective nonlinear plots of LM and FM, while Figure 6c illustrates the DRM investigations of INCR adsorption onto $MgAl_2O_4$-3, and the three models' findings are presented in Table 4. The fitting outcomes showed that INCR sorption onto $MgAl_2O_4$-3 agreed more with the LM, which predicted the capability of 1 g of $MgAl_2O_4$-3 to remove up to 181.278 mg INCR. Also, the less than unity value of $1/n$ implied that INCR sorption onto $MgAl_2O_4$-3 is favorable,[36] and the E_D value of 0.058 kJ mol^{-1} suggested that $MgAl_2O_4$-3 removed INCR via physisorption, which considered the positive outcome since it implied the ease of $MgAl_2O_4$-3 regeneration.[37]

Table 4. Isotherms and Thermodynamic Results of INCR Sorption by $MgAl_2O_4$-3 in the Concentration Range of 20 to 100 mg L^{-1}

adsorption isotherms										
isotherm model →	Langmuir			Freundlich			DRM			
temperature	R^2	K_L	q_m	R^2	K_f	$1/n$	q_m	K_{DR}	E	R^2
293 K	0.933	0.008	181.278	0.867	2.373	0.773	74.301	146.153	0.058	0.786

thermodynamic results							
conc. (mg L^{-1})	$\Delta H°$	$\Delta S°$	$\Delta G°$ (293 K)	$\Delta G°$ (303 K)	$\Delta G°$ (313 K)	$\Delta G°$ (323 K)	R^2
20.0	93.142	0.310	0.842	−2.255	−5.353	−8.450	1.000
40.0	61.670	0.201	1.771	−0.239	−2.250	−4.260	0.920
60.0	50.793	0.166	1.243	−0.419	−2.082	−3.745	0.971
80.0	33.388	0.108	1.318	0.242	−0.834	−1.910	0.983
100.0	30.111	0.094	1.963	1.019	−0.074	−0.871	0.949

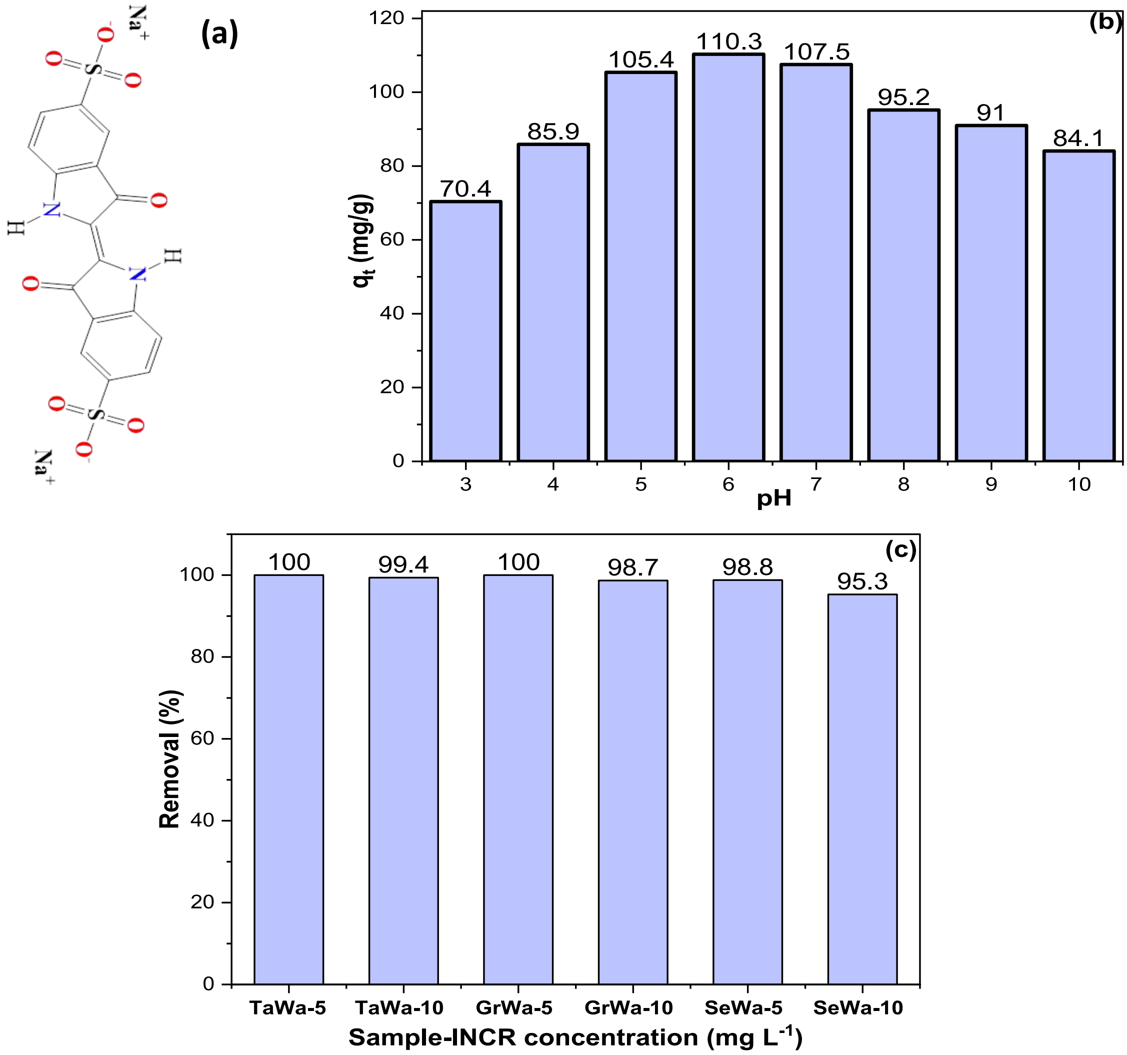

Figure 7. (a) INCR structure, (b) pH impact on INCR sorption onto $MgAl_2O_4$-3, and (c) application of $MgAl_2O_4$-3 for decontaminating natural water samples spiked with INCR to obtain 5 and 10 mg L^{-1} concentrations.

Furthermore, thermodynamics was examined to enhance the comprehension of INCR adsorption onto $MgAl_2O_4$-3. The results of INCR removal from the aforementioned concentrations at 293, 303, 313, and 323 K were employed for that purpose. The entropy ($\Delta S°$) and enthalpy ($\Delta H°$) values were computed from the plot of eq 16 (Figure 6d). At the same time, the Gibbs free energy ($\Delta G°$) was calculated from the difference in entropy and enthalpy values, computed using eq 17, and the thermodynamic outcomes are presented in Table 4.

$$\ln K_c = \frac{\Delta H°}{RT} + \frac{\Delta S°}{R} \tag{16}$$

$$\Delta G° = \Delta H° - T\Delta S° \tag{17}$$

https://doi.org/10.1021/acsomega.4c10353
ACS Omega 2025, 10, 11188−11201

The positive $\Delta H°$ and $\Delta G°$ values at 293 K reflected that the INCR sorption by $MgAl_2O_4$-3 was endothermic and nonspontaneous within all tested INCR concentrations. Elevating the temperature to 313 and 323 K shifted the INCR adsorption by $MgAl_2O_4$-3 and became spontaneous. The rise in the negative $\Delta G°$ values with decreasing initial concentration is promising for utilizing these sorbents in water treatment applications, mainly when dealing with low pollutant concentrations. The sorption of INCR onto $MgAl_2O_4$-3 being endothermic may be considered a drawback for cold countries, where heat sources might be used to optimize the sorption process.

3.4. Effect of pH. Generally, the solution pH substantially impacts the sorbent's polarity and electron availability, which influence the occurrence of electrostatic attraction or repulsion between the sorbent and sorbate, thereby having a crucial impact on the sorbent's ability to remove contaminants. The INCR featured several polar sites, such as carbonyl, amine, and sulfonic acid groups, with a sum of eight oxygen and two nitrogen atoms, which were considered electron-rich and partially negative sites (Figure 7a). Therefore, the influence of pH on INCR sorption by the $MgAl_2O_4$-3 quadruple nanocomposite was investigated. Figure 7b depicts pH 6.0 as suitable for INCR removal on $MgAl_2O_4$-3. Under high alkaline conditions, a competition for $MgAl_2O_4$-3 active sites might take place between INCR and the highly available ^{-}OH; furthermore, INCR molecules might be repelled by their electron-rich groups from the ^{-}OH on the $MgAl_2O_4$-3 surface. These suggestions might explain the drop in the sorption efficiency above pH 7.0. On the other hand, at low pH, where H^+ is abundant around $MgAl_2O_4$-3, it is expected to be protonated and occupy the electron-rich sites of INCR, resulting in its repulsion from the $MgAl_2O_4$-3 surface. While both excessive acidity and extreme alkalinity were disadvantageous, the highly alkaline environment exhibited less retardation of the INCR sorption process than the extremely acidic conditions.

3.5. Application to Natural Water Samples. The natural samples of TaWa, GrWa, and SeWa showed TDS values of 0.46, 0.89, and 33.28 g L^{-1}, respectively; their temperatures were 24.5, 25.5, and 25.5 °C, with pH values of 6.8, 7.3, and 6.5, respectively. The natural water pH was close enough to the optimum pH; therefore, the samples were treated as-obtained from their sources with a heating step (40 °C) to facilitate the sorption, as indicated by the thermodynamic results. Figure 7c shows the monitored efficiency of $MgAl_2O_4$-3 in removing INCR from GrWa and SeWa. The slight reduction in the removal of INCR from SeWa compared to that from TaWa and GrWa can be attributed to the elevated saline concentration in SeWa, which may block some $MgAl_2O_4$-3 active sorption sites and/or slow the INCR solution diffusion movement toward the $MgAl_2O_4$-3 surface.

4. CONCLUSIONS

In this study, $MgAl_2O_4$-based quadruple nanocomposites were prepared as a low-cost, environmentally friendly sorbent by using GLN as a green capping agent through a one-pot method. Typically, $MgAl_2O_4$-1, $MgAl_2O_4$-2, $MgAl_2O_4$-3, and $MgAl_2O_4$-4 were synthesized, which showed average particle sizes of 8.5, 7.6, 2.8, and 6.5 nm, respectively, with size ranges of 3.8−28.7, 1.7−26.0, 1.4−13.3, and 2.8−17.6 nm, respectively. The $MgAl_2O_4$-1, $MgAl_2O_4$-2, $MgAl_2O_4$-3, and $MgAl_2O_4$-4 nanocomposites showed surface areas of 75.409, 118.465, 141.073, and 122.984 m^2 g^{-1}, respectively, reflected as q_t values of 46.8, 60.9, 72.43, and 60.2 mg g^{-1}, respectively, within a time frame of 90 min. It is essential to mention that pH 6.0 is suitable for INCR removal on $MgAl_2O_4$-3. Kinetically, the INCR sorption onto $MgAl_2O_4$-1, $MgAl_2O_4$-2, $MgAl_2O_4$-3, and $MgAl_2O_4$-4 illustrated better agreement with the NLPS, and the LD exhibited significant control on INCR sorption by the quadruple nanocomposites with higher R^2 values and the X^2 and RSS of the LD being less than those of ID by about 50- to 200-fold. Moreover, the C_i values above zero for the four nanocomposites are an additional factor implying the sorption disagreement with the ID model. The q_t increased proportionally with 20 to 80 mg L^{-1} INCR concentrations. Line inflation was observed with 100 mg L^{-1}, indicating that the sorbent is suitable for treating up to 80 mg L^{-1} with typical solution-sorbent doses. Increasing the INCR solution temperature from 293 to 323 K increased the INCR removal efficiency from 44 to 96% for 20 mg L^{-1}, q_t of 100 mg L^{-1} from 58.9 to 110.6 mg g^{-1}, indicating cluster disintegration and virgin active sorption site liberation; thus, the sorption is endothermic. The INCR sorption at 293 K transformed spontaneously when INCR-contaminated water was heated to 313 K. The $\Delta G°$ values became more negative with 20 mg L^{-1} INCR concentration, nominating $MgAl_2O_4$-3 for treating polluted water resources where low INCR concentrations are anticipated. The reduction of $\Delta G°$ values as the initial INCR concentration decreases is considered promising for employing $MgAl_2O_4$-3 in water treatment applications where INCR concentrations are low. The natural water samples TaWa, GrWa, and SeWa were treated without pH adjustment as they were close enough to the optimum pH. The INCR removal was conducted at 313 K, as indicated by the thermodynamic results, and the $MgAl_2O_4$-3 exhibited an average removal of 97.1% with a range of 95.4−100% and a standard deviation of 2.4%. Even though the efficiency of $MgAl_2O_4$-3 decreased with seawater by about 5%, this does not indicate a lack of $MgAl_2O_4$-3 excellency, as the high salt content of seawater adversely affects the INCR diffusion and/or blocks $MgAl_2O_4$-3 sites. It might be unreasonable to generalize the superb performance of $MgAl_2O_4$-3 in removing INCR to all organic pollutants, but it is rational to expect anionic dyes to be eliminated efficiently using $MgAl_2O_4$-3.

■ ASSOCIATED CONTENT

Data Availability Statement

The data generated in this study are included in the paper, and any additional information about the raw data can be provided by the corresponding author.

■ AUTHOR INFORMATION

Corresponding Author

Sondos A. J. Almahmoud − *Chemistry Department, College of Science, Imam Mohammad Ibn Saud Islamic University (IMSIU), Riyadh 11623, Saudi Arabia;* orcid.org/0000-0003-4941-7192; Email: salmahmoud@imamu.edu.sa

Authors

Soad S. Alzahrani − *Chemistry Department, College of Science, Imam Mohammad Ibn Saud Islamic University (IMSIU), Riyadh 11623, Saudi Arabia;* orcid.org/0000-0002-3395-181X

Babiker Y. Abdulkhair − *Chemistry Department, College of Science, Imam Mohammad Ibn Saud Islamic University (IMSIU), Riyadh 11623, Saudi Arabia*

Complete contact information is available at:
https://pubs.acs.org/10.1021/acsomega.4c10353

Funding

This work was supported and funded by the Deanship of Scientific Research at Imam Mohammad Ibn Saud Islamic University (IMSIU) (grant number IMSIU-DDRSP2502).

Notes

The authors declare no competing financial interest.

■ ACKNOWLEDGMENTS

The authors acknowledge the Deanship of Scientific Research at Imam Mohammad Ibn Saud Islamic University (IMSIU).

■ REFERENCES

(1) Almufarij, R. S.; Abdulkhair, B. Y.; Salih, M.; Alhamdan, N. M. Sweep-Out of Tigecycline, Chlortetracycline, Oxytetracycline, and Doxycycline from Water by Carbon Nanoparticles Derived from Tissue Waste. *Nanomaterials* **2022**, *12* (20), No. 3617.

(2) (a) Ristea, M.-E.; Zarnescu, O. Indigo Carmine: Between Necessity and Concern. *J. Xenobiot.* **2023**, *13* (3), 509−528. (b) Komboonchoo, S.; Bechtold, T. Natural dyeing of wool and hair with indigo carmine (C.I. Natural Blue 2), a renewable resource based blue dye. *J. Cleaner Prod.* **2009**, *17* (16), 1487−1493.

(3) Chowdhury, M. F.; Khandaker, S.; Sarker, F.; Islam, A.; Rahman, M. T.; Awual, M. R. Current treatment technologies and mechanisms for removal of indigo carmine dyes from wastewater: A review. *J. Mol. Liq.* **2020**, *318*, No. 114061.

(4) Babu, A. N.; Reddy, D. S.; Sharma, P.; Kumar, G. S.; Ravindhranath, K.; Mohan, G. V. K. Removal of Hazardous Indigo Carmine Dye from Waste Water Using Treated Red Mud. *Mater. Today: Proc.* **2019**, *17*, 198−208.

(5) Pereira, P. C. G.; Reimão, R. V.; Pavesi, T.; Saggioro, E. M.; Moreira, J. C.; Correia, F. V. Lethal and sub-lethal evaluation of Indigo Carmine dye and byproducts after TiO2 photocatalysis in the immune system of Eisenia andrei earthworms. *Ecotoxicol. Environ. Saf.* **2017**, *143*, 275−282.

(6) Elamin, M. R.; Abdulkhair, B. Y.; Elzupir, A. O. Removal of ciprofloxacin and indigo carmine from water by carbon nanotubes fabricated from a low-cost precursor: Solution parameters and recyclability. *Ain Shams Eng. J.* **2023**, *14* (1), No. 101844.

(7) Linke, J. A.; Rayat, A.; Ward, J. M. Production of indigo by recombinant bacteria. *Bioresour. Bioprocess.* **2023**, *10* (1), No. 20.

(8) Babu, A. N.; Reddy, D. S.; Sharma, P.; Kumar, G. S.; Ravindhranath, K.; Mohan, G. K. Removal of hazardous indigo carmine dye from waste water using treated red mud. *Mater. Today: Proc.* **2019**, *17*, 198−208.

(9) (a) Paul, R.; Blackburn, R. S.; Bechtold, T.Indigo and Indigo Colorants. In *Ullmann's Encyclopedia of Industrial Chemistry*; Wiley, 2000; pp 1−16. (b) Abdulkhair, B. Y.; Elamin, M. R. Low-cost carbon nanoparticles for removing hazardous organic pollutants from water: complete remediation study and multi-use investigation. *Inorganics* **2022**, *10* (9), No. 136.

(10) Rodríguez-Couto, S.; Osma, J. F.; Toca-Herrera, J. L. Removal of synthetic dyes by an eco-friendly strategy. *Eng. Life Sci.* **2009**, *9* (2), 116−123.

(11) (a) Elamin, M. R.; Ibnaouf, K. H.; Elamin, N. Y.; Adam, F. A.; Alolayan, A. H.; Abdulkhair, B. Y. Spontaneous Adsorption and Efficient Photodegradation of Indigo Carmine under Visible Light by Bismuth Oxyiodide Nanoparticles Fabricated Entirely at Room Temperature. *Inorganics* **2022**, *10* (5), No. 65. (b) Kuncser, A. C.; Rostas, A. M.; Zavoianu, R.; Pavel, O. D.; Vlaicu, I. D.; Badea, M.; Culita, D. C.; Tirsoaga, A.; Olar, R. Synthesis and characterization of hematite-based nanocomposites as promising catalysts for indigo carmine oxidation. *Nanomaterials* **2022**, *12* (14), No. 2511. (c) Fallah, N.; Bloise, E.; García-López, E. I.; Mele, G. Carbon-Based Materials in Combined Adsorption/Ozonation for Indigo Dye Decolorization in Constrain Contact Time. *Molecules* **2024**, *29* (17), No. 4144.

(12) Naseem, T.; Durrani, T. The role of some important metal oxide nanoparticles for wastewater and antibacterial applications: A review. *Environ. Chem. Ecotoxicol.* **2021**, *3*, 59−75.

(13) Hosny, N. M.; Gomaa, I.; Elmahgary, M. G. Adsorption of polluted dyes from water by transition metal oxides: A review. *Appl. Surf. Sci. Adv.* **2023**, *15*, No. 100395.

(14) Dabhade, G.; Daware, G.; Rajesh, Y.; Jeeru, L. R. An efficient removal of Indigo Carmine dye (IC) from aqueous medium using environmental friendly synthesized ZnAl2O4. *Mater. Today: Proc.* **2023**, *77*, 54−59.

(15) Helali, S.; Rashad, M.; Mabrouk, A. B.; Alanazi, M. A. A.; Mustafa, M. S. Structural Analysis and Adsorption Studies of (PbO, MgO) Metal Oxide Nanocomposites for Efficient Methylene Blue Dye Removal from Water. *Materials* **2024**, *17* (12), No. 2890, DOI: 10.3390/ma17122890.

(16) (a) Almufarij, R. S.; Abdulkhair, B. Y.; Salih, M. Fast-simplistic fabrication of MoO3@Al2O3-MgO triple nanocomposites for efficient elimination of pharmaceutical contaminants. *Results Chem.* **2024**, *7*, No. 101281. (b) Khairy, M.; Algethami, F. K.; Alotaibi, A. N.; Almufarij, R. S.; Abdulkhair, B. Y. Enhancing the Conductivity and Dielectric Characteristics of Bismuth Oxyiodide via Activated Carbon Doping. *Molecules* **2024**, *29* (9), No. 2082. (c) Algethami, F. K.; Elamin, M. R.; Abdulkhair, B. Y.; Al-Zharani, M.; Qarah, N. A.; Alghamdi, M. A. Fast fabrication of bismuth oxyiodide/carbon-nanofibers composites for efficient anti-proliferation of liver and breast cancer cells. *Z. Anorg. Allg. Chem.* **2021**, *647* (19), 1921−1929.

(17) Ma, X.; Zhu, Z.; Wu, J.; Wei, H.; Gong, C.; Yoriya, S.; He, P.; Luo, G.; Yao, H. Structural reconfiguration of Al/CaO adsorbent by Ni doping to improve sintering resistance and arsenic removal performance. *Appl. Surf. Sci.* **2024**, *652*, No. 159325.

(18) (a) Dousset, V.; Grossman, R. I.; Ramer, K. N.; Schnall, M. D.; Young, L. H.; Gonzalez-Scarano, F.; Lavi, E.; Cohen, J. A. Experimental allergic encephalomyelitis and multiple sclerosis: lesion characterization with magnetization transfer imaging. *Radiology* **1992**, *182* (2), 483−491. (b) Kathiravan, P.; Thillaivelavan, K.; Viruthagiri, G. Influence of Cu-ion doping in NiO NPs and their structural, morphological, optical and magnetic behaviors for optoelectronic devices and magnetic applications. *Spectrochim. Acta, Part A* **2024**, *308*, No. 123745. (c) Sun, P.-P.; Zhang, Y.-H.; Pan, G.-X.; Yu, X.; Shi, Q.; Tian, B.; Gao, J.; Shi, F.-N. Application of NiO-modified NiCo2O4 hollow spheres for high performance lithium ion batteries and supercapacitors. *J. Alloys Compd.* **2020**, *832*, No. 154954.

(19) Salaheldin, H. I.; Almalki, M. H. K.; Osman, G. E. H. Green synthesis of silver nanoparticles using bovine skin gelatin and its antibacterial effect on clinical bacterial isolates. *IET Nanobiotechnol.* **2017**, *11* (4), 420−425.

(20) (a) Darroudi, M.; Ahmad, M. M. B.; Abdullah, A. H.; Ibrahim, N. A.; Shameli, K. Green synthesis and characterization of gelatin-based and sugar-reduced silver nanoparticles. *Int. J. Nanomed.* **2011**, *6*, 569−574. From NLM. (b) Salem, M. S.; Elmarghany, M. R.; Salem, N.; Nady, N. Synthesis of Urchin-Shaped Gold Nanoparticles Utilizing Green Reducing and Capping Agents at Different Preparation Conditions: An In Vitro Study. *Sustainability* **2022**, *14* (24), No. 16838.

(21) (a) Milani, S. S.; Kakroudi, M. G.; Vafa, N. P.; Rahro, S.; Behboudi, F. Synthesis and characterization of MgAl2O4 spinel precursor sol prepared by inorganic salts. *Ceram. Int.* **2021**, *47* (4), 4813−4819. (b) Mahmoud, S. A.; Elsisi, M. E.; Mansour, A. F. Synthesis and electrochemical performance of α-Al2O3 and M-Al2O4 spinel nanocomposites in hybrid quantum dot-sensitized solar cells. *Sci. Rep.* **2022**, *12* (1), No. 17009.

(22) Thommes, M.; Kaneko, K.; Neimark, A. V.; Olivier, J. P.; Rodriguez-Reinoso, F.; Rouquerol, J.; Sing, K. S. Physisorption of gases, with special reference to the evaluation of surface area and pore

size distribution (IUPAC Technical Report). *Pure Appl. Chem.* **2015**, *87* (9−10), 1051−1069.

(23) Almufarij, R. S.; Abdulkhair, B. Y.; Salih, M. Fast-simplistic fabrication of MoO3@ Al2O3-MgO triple nanocomposites for efficient elimination of pharmaceutical contaminants. *Results Chem.* **2024**, *7*, No. 101281.

(24) Pei, L.-Z.; Yin, W.-Y.; Wang, J.-F.; Chen, J.; Fan, C.-G.; Zhang, Q.-F. Low temperature synthesis of magnesium oxide and spinel powders by a sol-gel process. *Mater. Res.* **2010**, *13*, 339−343.

(25) Bhowmik, S.; Chakraborty, V.; Das, P. Batch adsorption of indigo carmine on activated carbon prepared from sawdust: A comparative study and optimization of operating conditions using Response Surface Methodology. *Results Surf. Interfaces* **2021**, *3*, No. 100011.

(26) Tabi, G. A.; Blaise, L. N. R.; Daouda, K.; Odogu, A. N.; Victoire, A. A.; Julius, N. N.; Mbadcam, K. J. Non-linear modelling of the adsorption of Indigo Carmine dye from wastewater onto characterized activated carbon/volcanic ash composite. *Arabian J. Chem.* **2022**, *15* (1), No. 103515.

(27) Harrache, Z.; Abbas, M.; Aksil, T.; Trari, M. Thermodynamic and kinetics studies on adsorption of Indigo Carmine from aqueous solution by activated carbon. *Microchem. J.* **2019**, *144*, 180−189.

(28) Khadhri, N.; Saad, M. E. K.; Mosbah, M. b.; Moussaoui, Y. Batch and continuous column adsorption of indigo carmine onto activated carbon derived from date palm petiole. *J. Environ. Chem. Eng.* **2019**, *7* (1), No. 102775.

(29) El-Kammah, M.; Elkhatib, E.; Gouveia, S.; Cameselle, C.; Aboukila, E. Enhanced removal of Indigo Carmine dye from textile effluent using green cost-efficient nanomaterial: Adsorption, kinetics, thermodynamics and mechanisms. *Sustainable Chem. Pharm.* **2022**, *29*, No. 100753.

(30) Nindjio, G. F. K.; Tagne, R. F. T.; Jiokeng, S. L. Z.; Fotsop, C. G.; Bopda, A.; Doungmo, G.; Temgoua, R. C. T.; Doench, I.; Njoyim, E. T.; Tamo, A. K.; et al. Lignocellulosic-based materials from bean and pistachio pod wastes for dye-contaminated water treatment: optimization and modeling of indigo carmine sorption. *Polymers* **2022**, *14* (18), No. 3776.

(31) Ismail, B.; Hussain, S. T.; Akram, S. Adsorption of methylene blue onto spinel magnesium aluminate nanoparticles: adsorption isotherms, kinetic and thermodynamic studies. *Chem. Eng. J.* **2013**, *219*, 395−402.

(32) Yin, S.; López, J. F.; Solís, J. J. C.; Wong, M. S.; Villagrán, D. Enhanced adsorption of PFOA with nano MgAl2O4@ CNTs: influence of pH and dosage, and environmental conditions. *J. Hazard. Mater. Adv.* **2023**, *9*, No. 100252.

(33) Elamin, M. R.; Abdulkhair, B. Y.; Algethami, F. K.; Khezami, L. Linear and nonlinear investigations for the adsorption of paracetamol and metformin from water on acid-treated clay. *Sci. Rep.* **2021**, *11* (1), No. 13606.

(34) Mallakpour, S.; Tabesh, F. Tragacanth gum based hydrogel nanocomposites for the adsorption of methylene blue: Comparison of linear and non-linear forms of different adsorption isotherm and kinetics models. *Int. J. Biol. Macromol.* **2019**, *133*, 754−766.

(35) An, B. Cu (II) and As (V) adsorption kinetic characteristic of the multifunctional amino groups in chitosan. *Processes* **2020**, *8* (9), No. 1194.

(36) Ibrahim, T. G.; Almufarij, R. S.; Abdulkhair, B. Y.; Ramadan, R. S.; Eltoum, M. S.; Elaziz, M. E. A. A Thorough Examination of the Solution Conditions and the Use of Carbon Nanoparticles Made from Commercial Mesquite Charcoal as a Successful Sorbent for Water Remediation. *Nanomaterials* **2023**, *13* (9), No. 1485.

(37) Chaouati, N.; Soualah, A.; Chater, M. Adsorption of phenol from aqueous solution onto zeolites Y modified by silylation. *C. R. Chim.* **2013**, *16* (3), 222−228.